

Refractive errors and corrections for OCT images in an inflated lung phantom

Ali Golabchi,¹ J. Faust,² F. N. Golabchi,¹ D. H. Brooks,¹
A. Gouldstone,^{2,*} and C. A. DiMarzio^{1,2,3}

¹Electrical and Computer Engineering Department, Northeastern University, Boston, MA 02115, USA

²Mechanical Engineering Department, Northeastern University, Boston, MA 02115, USA

³Bernard M. Gordon Center for Subsurface Sensing and Imaging Systems (CenSSIS), Boston, MA 02115, USA

*a.gouldstone@neu.edu

Abstract: Visualization and correct assessment of alveolar volume *via* intact lung imaging is important to study and assess respiratory mechanics. Optical Coherence Tomography (OCT), a real-time imaging technique based on near-infrared interferometry, can image several layers of distal alveoli in intact, *ex vivo* lung tissue. However optical effects associated with heterogeneity of lung tissue, including the refraction caused by air-tissue interfaces along alveoli and duct walls, and changes in speed of light as it travels through the tissue, result in inaccurate measurement of alveolar volume. Experimentally such errors have been difficult to analyze because of lack of 'ground truth,' as the lung has a unique microstructure of liquid-coated thin walls surrounding relatively large airspaces, which is difficult to model with cellular foams. In addition, both lung and foams contain airspaces of highly irregular shape, further complicating quantitative measurement of optical artifacts and correction. To address this we have adapted the Bragg-Nye bubble raft, a crystalline two-dimensional arrangement of elements similar in geometry to alveoli (up to several hundred μm in diameter with thin walls) as an inflated lung phantom in order to understand, analyze and correct these errors. By applying exact optical ray tracing on OCT images of the bubble raft, the errors are predicted and corrected. The results are validated by imaging the bubble raft with OCT from one edge and with a charged coupled device (CCD) camera in transillumination from top, providing ground truth for the OCT.

© 2012 Optical Society of America

OCIS codes: (080.0080) Geometric optics; (080.2710) Inhomogeneous optical media; (100.2960) Image analysis; (170.5380) Physiology

References and links

1. I. A. Greaves, J. Hildebrandt, and F. G. Hoppin, "Micromechanics of the lung," *Comprehensive Physiol.* **2011**, 217–231 (2011).
2. K.F. Udobi, E. Childs, and K. Touijer, "Acute respiratory distress syndrome," *Am. Family Physician*, **67**, 315–322 (2003).
3. D. Dreyfuss and G. Saumon, "Ventilator-induced lung injury: lessons from experimental studies," *Respir. Crit. Care Med.* **157**, 294–323 (1998).
4. D. E. O'Donnell, S. M. Revill, and K. A. Webb, "Dynamic hyperinflation and exercise intolerance in chronic obstructive pulmonary disease," *Am. J. Respir. Crit. Care Med* **165**(5), 770-777 (2001).

5. D. Carney, J. DiRocco, and G. Nieman, "Dynamic alveolar mechanics and ventilator-induced lung injury," *Crit. Care Med.* **33**, S122–S128 (2005).
6. A. Sarnaik, K. Daphtary, K. Meert, M. Lieh-Lai, and S. Heidemann, "Pressure-controlled ventilation in children with severe status asthmaticus," *Pediatr. Crit. Care Med.* **5**(2), 133–138 (2004).
7. A. Bashkatov, E. Genina, and V. Tuchin, "Tissue optical properties," in *Handbook of Biomedical Optics* (CRC Press, 2011), pp. 67–100.
8. W. C. Warger, C. A. DiMarzio, and M. Rajadhyaksha, "Confocal microscopy," in *Handbook of Biomedical Optics* (CRC Press, 2011), pp. 517–542.
9. H. Choi, J. Cha, and P. So, "Nonlinear optical microscopy for biology and medicine," in *Handbook of Biomedical Optics* (CRC Press, 2011), pp. 561–588.
10. F. E. Ben-Isaac and D. H. Simmons, "Flexible fiberoptic pleuroscopy: pleural and lung biopsy," *CHEST* **67**(5), 573–576.
11. D. Huang, E. A. Swanson, C. P. Lin, J. S. Schuman, W. G. Stinson, W. Chang, M. R. Hee, T. Flotte, K. Gregory, and C. A. Puliafito, "Optical coherence tomography," *Science* **254**, 1178–1181 (1991).
12. A. Popp, M. Wendel, L. Knels, T. Koch, and E. Koch, "Imaging of the three-dimensional alveolar structure and the alveolar mechanics of a ventilated and perfused isolated rabbit lung with Fourier domain optical coherence tomography," *J. Biomed. Opt.* **11**, 014015 (2006).
13. S. Meissner, L. Knels, A. Krueger, T. Koch, and E. Koch, "Simultaneous three-dimensional optical coherence tomography and intravital microscopy for imaging subpleural pulmonary alveoli in isolated rabbit lungs," *Eu. Respir. J.* **14**, 054020 (2009).
14. N. Hanna, D. Saltzman, D. Mukai, Z. Chen, S. Sasse, J. Milliken, S. Guo, W. Jung, H. Colt, and M. Brenner, "Two-dimensional and 3-dimensional optical coherence tomographic imaging of the airway, lung, and pleura," *J. Thoracic Cardiovascular Surg.* **129**, 615–622 (2005).
15. A. Gouldstone, N. Caner, T. B. Swedish, S. M. Kalkhoran, and C. A. Dimarzio, "Mechanical and optical dynamic model of lung," *IEEE Trans. Biomed. Eng.* **58**, 3012–3015 (2011).
16. M. R. Silva, H. T. Shen, A. Marzban, and A. Gouldstone, "Instrumented indentation of lung reveals significant short term alteration in mechanical behavior with 100 percent oxygen," *Healthcare Eng.* **1**, 415–434 (2010).
17. M. R. Silva, Z. Yuan, J. H. Kim, Z. Wang, M. Hoyos, Y. Pan, and A. Gouldstone, "Spherical indentation of lungs: experiments, modeling and sub-surface imaging," *J. Mater. Res.* **24**, 1156–1166 (2009).
18. S. Meissner, L. Knels, C. Schnabel, T. Koch, and E. Koch, "Improved three-dimensional Fourier domain optical coherence tomography by index matching in alveolar structures," *J. Biomed. Opt.* **14**, 064037 (2009).
19. M. Chen, Y. C. Yortsos, and W. R. Rossen, "Pore-network study of the mechanisms of foam generation in porous media," *X. Phys. Rev. E* **73**, 036304 (2006).
20. A. van der Net, G. W. Delaney, W. Drenckhan, D. Weaire, and S. Hutzler, "Crystalline arrangements of microbubbles in monodisperse foams," *Colloids Surfaces A: Physicochem. Eng. Aspects* **309**(1–3), 117–124 (2007).
21. L. Bragg and J. F. Nye, "A dynamical model of a crystal structure," *Proc. R. Soc. Lond. A* **190**, 474–481 (1947).
22. F. N. Golabchi, D. H. Brooks, A. Gouldstone, and C. A. Dimarzio, "Refractive effects on optical measurement of alveolar volume: a 2-D ray tracing approach," in *Proceedings of IEEE Conference on Engineering in Medicine and Biology Society*, (IEEE, 2011), pp. 7771–7774.
23. D. C. Reed and C. A. DiMarzio, "Computational model of OCT in lung tissue," *Proc. SPIE* **7570**, 75700I (2010).
24. T. B. Swedish, J. P. Robinson, M. R. Silva, A. Gouldstone, D. Kaeli, and C. A. DiMarzio, "Computational model of optical scattering by elastin in lung," *Proc. SPIE* **7004**, 79040H (2011).

1. Introduction

Lung imaging is important for lung physiology and pathology. For example accurate measurement of alveolar volume under different environmental or clinical conditions can provide information about the stability, interdependence, and mechanism of alveolar collapse and re-opening specifically under mechanical ventilation or condition of atelectatic recovery [1]. Serious pathologies associated with sub-optimal mechanical behavior of the lung include acute respiratory distress syndrome (ARDS)[2], chronic obstructive pulmonary disease (COPD)[4], ventilator-induced lung injury (VILI)[3, 5] and extreme cases of asthma[6]. Accordingly, improved knowledge of lung mechanics, from pressure-volume compliance to alveolar collapse and re-opening, can provide insight into the initiation and progression of such pathologies.

The intact lung is a particularly difficult organ to observe. At one scale, macroscopic imaging techniques are limited by the small size of the important structures such as alveoli, capillaries and alveolar walls. Although light penetrates a considerable distance into lung[7] and changes

in reflected light can be observed in response to changes in pressure or external forces, these observations do not provide information about the behavior of individual alveoli and membranes. At a smaller scale, optical microscopy through the pleura is adversely affected by the optical heterogeneity of lungs primarily because of the high air-tissue contrast in indices of refraction, and image quality measures such as resolution, contrast and distortion of morphological features, degrade with depth. In other organs, these problems can be mitigated through direct imaging of excised tissue samples. The lung, however, collapses under biopsy[10]; thus while histological images of lung can be representative of *in vivo* static structure if painstakingly prepared, they cannot preserve *in vivo* dynamics.

Optical Coherence Tomography (OCT)[11], a real-time imaging technique based on near-infrared interferometry, can image up to several layers of distal alveoli in lung tissue [12, 13]. OCT provides better penetration depth, at some cost in transverse resolution in comparison with microscopy imaging techniques such as confocal and multi-photon that rely on rejection of strongly scattered light through direct spatial filtering, or non-linear effects[8, 9]. OCT imaging rejects scattered light through temporal filtering, and has been successful at resolving alveolar structures [12, 14, 15]. Looking at artificially inflated lung on the microscale utilizing OCT can provide useful information about the changes in its mechanical and morphological properties *ex vivo* [16, 17].

OCT is based on the calculation of distance based on travel time assuming a known speed and in-line reflection. Thus, refractive effects from air-tissue interfaces inside the lung result in errors in optical measurement of alveolar volume (area, in 2D) during OCT imaging. In addition, heterogeneities in the alveolar tissue walls produce errors in OCT reconstructions, due to changes in the speed of light. Thus, both refractive changes in angle and discrepancies between the assumed speed of light in air and its actual speed through the tissue lead to distortion in reconstructed OCT images. Filling the lung with index-matching liquid greatly improves images [18], but may have limitations in studies of *in-situ* alveolar dynamics, for example under re-inflation. Imaging errors in air-filled lung can be modeled, but the complex microstructure of alveoli makes validation challenging as it is difficult to know whether a 'correct' (e.g., fixed histology) sample is the same as the OCT image. Even if such confidence is achieved, the irregularities in alveolar geometry make errors difficult to quantify. Note that this problem can also arise in other types of delicate, highly porous media including liquid foams[19, 20].

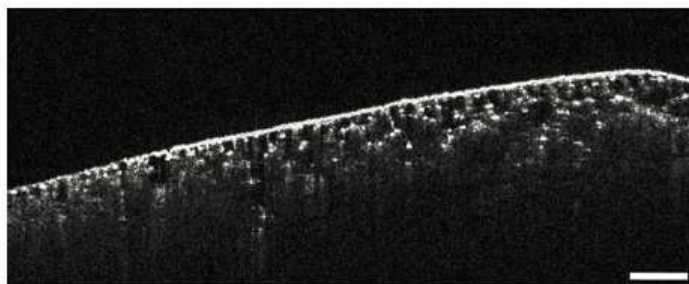


Fig. 1. OCT image of inflated rat lung, showing several layers of alveoli in cross-section. Scale bar is $500\mu\text{m}$ [17]. © Materials Research Society 2009—reprinted with permission.

Thus, there is need for a lung phantom for experimental validation of optical effects in lung, that includes (i) air-scattering medium interfaces, (ii) similar geometry (wall thickness to airspace diameter), (iii) a highly repeatable simple structure and (iv) the ability to control optical properties. Cellular foams and fixed lung samples do not provide all these capabilities. Accordingly, in this study we adapted a Bragg Nye bubble raft, a hexagonal crystalline

arrangement of sub- μm diameter bubbles, previously used in experimental atomic simulations [21] and imaged it using OCT. Note that in all previous bubble raft works, dynamic atomistic models were performed. Here we only use the raft for its regular structure and bubble diameter-wall thickness ratio that is strikingly similar to that of lung, allowing us to model the optical heterogeneity between alveolar tissue and air spaces.

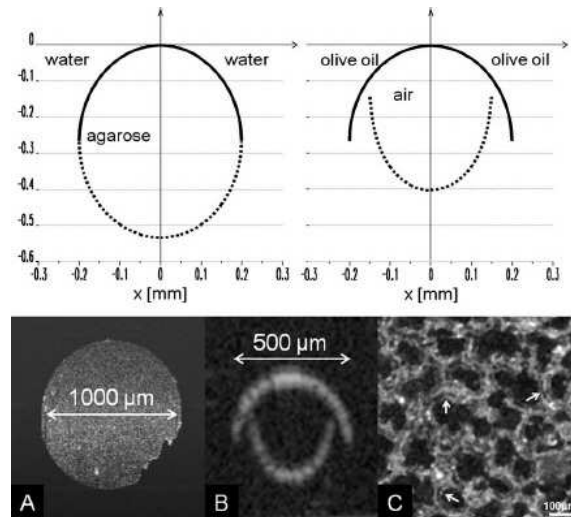


Fig. 2. Illustration of the artifacts in OCT images caused by air/tissue interfaces. Upper panel: simulated OCT cross sections of a turbid agarose gel stick (left) and air bubble (right) surrounded by olive oil to demonstrate image generation for fluid and air-filled alveoli. OCT cross sections of the phantom measurements of (A) optical turbid agarose gel stick and (B) air bubble in olive oil. (C) OCT en-face image showing the artifacts caused by the air/tissue interfaces that result in pseudodoubled alveolar walls (white arrows). Image by Sven Meissner et al. (This figure is reproduced with permission from the *Journal of Biomedical Optics* and the authors [18].)

This is similar to an experiment reported by Meissner, et al [18] who demonstrated the artificial thickening of alveolar walls under OCT imaging (Fig. 2), due to the air-tissue interface, and modeled an alveolus using a single air bubble in olive oil. They observed particular artifacts, such as double wall effect. Compared to the single bubble the raft adds capabilities of a repeating structure, layer-by-layer effects and tailoring. After construction of a suitable raft we used a ray tracing approach [22] to calculate and correct the artifacts. OCT images (with artifacts) were compared with a 'gold standard' obtained, by simultaneous top-to-bottom transillumination CCD imaging of the raft along with the OCT from the side. The experimental setup is shown in Fig. 3.

2. Methods

2.1. Bubble raft

A bubble raft was made from a solution-mixture consisting of 100 ml distilled water, 3 ml dish soap and 15 ml whole milk. Milk was used to increase scattering effects under OCT and improve contrast to be comparable to that of lung. To produce bubbles, air was blown at a constant air pressure of approximately $28 \text{ cmH}_2\text{O}$, through a 31 gauge hypodermic needle with a 0.005 inch (0.127 mm) inner diameter placed approximately 0.5 cm below the surface of the soap solution. To improve uniformity and decrease average bubble diameter to $200 \mu\text{m}$, the solution was heated to 24°C and rotated, the latter method originally suggested by Bragg and Nye [21].

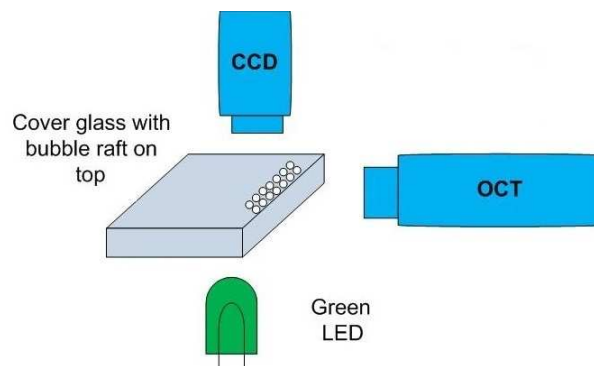


Fig. 3. Experimental setup - a bubble raft on a glass cover slip was imaged on edge by OCT, and from above by CCD. The raft was illuminated from below by a green LED to improve contrast in the CCD. For the experiment in this paper, the raft is a single layer of bubbles approximately $250\mu\text{m}$ thick.

The bubbles naturally formed a hexagonal arrangement on the liquid surface, and a stirring rod and heated wire were used to remove crystalline defects, again as reported previously [21]. A perfect flat edge was achieved by destroying outlying bubbles with a soldering iron. When a suitable raft was arranged, it was transferred to a glass laboratory slide (*via* scooping) to stabilize it for carrying to the OCT apparatus. As the bubbles were indistinguishable from each other under both OCT and CCD imaging, a negative fiducial marker was created when needed, by popping several bubbles on the edge.

2.2. Data acquisition

The bubble raft was imaged from the edge utilizing OCT and a CCD camera was used with normal orientation to the raft as shown in Fig. 3. The CCD setup was an Olympus E-P1 digital camera with an Olympus 14-42 mm lens and a M.U.K macro extension tube. To improve visibility, the raft was illuminated from below with a green LED. OCT images were taken from the edge of the raft utilizing a commercial standard SR-OCT (Thorlabs, Inc., Newton, NJ) with an imaging depth of 1.6 mm and axial resolution of 6.2 μm . CCD images and OCT images of the bubble raft used for the analysis are shown in Figs. 4a, b, and c respectively. Although there are qualitative similarities (e.g. periodicity, near-spherical walls), there are also significant differences, which are analyzed below.

2.3. Data processing

After the OCT image was acquired, it was registered to the corresponding CCD image manually, using a global affine transformation allowing only translation, rotation, and isotropic scaling so that the structure of the measurements stayed unchanged. The location of the top surface of the top layer of bubbles in the bubble raft was used as the landmark feature to be aligned in the two set of image data. This allowed both images to be registered into a common space, i.e., the CCD image space. Figs. 5a and b show the same bubble, simultaneously imaged via OCT and CCD, respectively. There are a few salient features, which are the foci of this paper. First, the top surface of the OCT bubble shows a wall of milk solution-mixture that is thicker than in the CCD image. Second, the bottom surface of the OCT bubble is disconnected from the top surface, and distorted, forming a double-wall image shown by an arrow in Fig. 5a. This effect has been previously reported in [18]. In this section we describe a means to predict the OCT artifacts, and correct for them, using methods outlined in [22].

A forward ray tracing model was used to predict the distorted measurements of the bottom

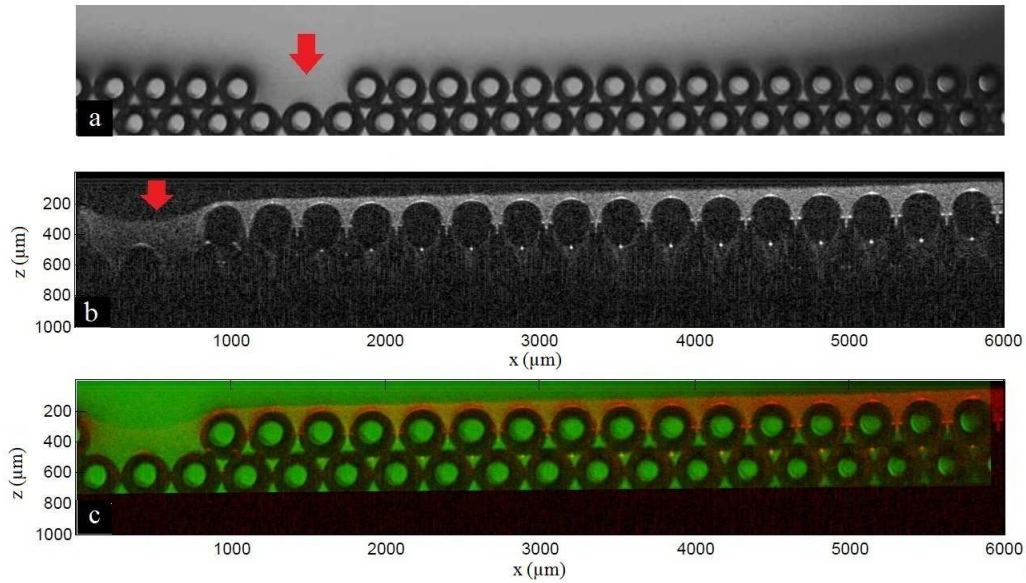


Fig. 4. Bubble raft imaged (a) from above via CCD and (b) from the edge using OCT. Arrows show popped bubbles used for matching in registration. (c) OCT (red plane) and CCD (green plane) images overlaid, via rotation, translation and isotropic scaling.

surface, using the correct measurements of the top surface, while assuming an ellipsoidal geometry for the entire bubble. The first step was to correct for the incorrect depth of the bubble top surface measured by the OCT signal, due to change in the index of refraction from air to liquid. Using the OCT measurements, the location of the top surface of the bubble was manually detected by selecting a finite number of points on locations where an edge in the bubble top surface was visible. The points were then fitted to an ellipse in a least square manner. The coordinates of the collection of points on the ellipse top surface are denoted by (X'_1, Z'_1) . In this step, the correction for the distortions that result from change in the speed of light in the milk solution was only required along the optical axis. Thus, the correct location of the points on the top surface were calculated by simply dividing the distance traveled between surface of the milk solution, denoted by Z_0 , and the top surface of the bubble measured by OCT, denoted by Z'_1 , by the index of refraction of the milk solution, $n = 1.33$ as shown below:

$$\begin{aligned} X_1 &= X'_1 \\ Z_1 &= Z_0 + (Z'_1 - Z_0)/n \end{aligned}$$

Once the corrected top surface was found, the bottom surface was analyzed. As stated in [22], the double wall artifact arises due to refractive effects that are not accounted for in OCT, and is schematized in Fig. 5c. When rays hit the bottom surface they are partially backscattered, re-tracing their original paths. However, OCT interprets these rays path as parallel to the optical axis, so while the distance traveled is conserved, the direction of origin is altered by the refraction angle. Thus, the reconstructed bottom surface appears distorted and disconnected.

After coordinates of the correct location of the top surface, (X_1, Z_1) , were found, inverse ray tracing was used to predict the correct location of the bottom surface using the locations of both top and bottom surface as measured by the OCT. First, using the OCT measurements the location of the bottom surface of the bubble was found in the same manner as the top surface

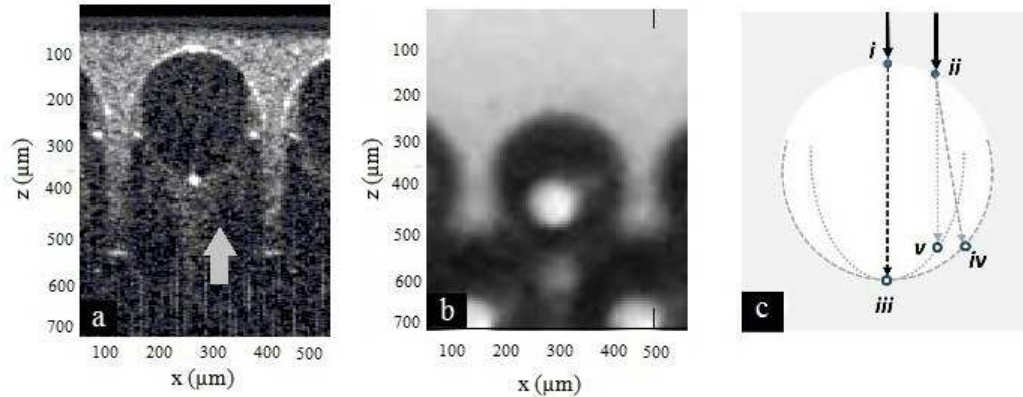


Fig. 5. (a) OCT image of a single bubble. Arrow points to 'double wall' artifact. (b) CCD image of the same bubble, with surrounding bubbles visible. Images are scaled to same size. (c) Model showing refractive effects on a single bubble of air (white) in a medium with higher refractive index (grey). A light ray (black line) crossing the medium-air interface at (i) is normal to the interface, and is not refracted, impinging on the bottom surface at (iii). This is backscattered to i and no artifact occurs. The light ray (grey line) crossing at (ii) is refracted to impinge the bottom surface (grey dashed arc) at (iv), where it is backscattered to (ii). However, the OCT system interprets this as a ray parallel to the optical axis (grey dotted line), thus "detecting" the bottom surface at (v). Rays refracted in this way lead to construction of the double wall (grey dotted arc.)

was found. The coordinates of the collection of points on the bottom surface are referred to as (X'_2, Z'_2) .

The points on the bottom surface of the bubble were projected to the correct location of the bubble top surface parallel to the optical (z) axis to find the point at which each ray met the liquid-air interface. Using Snell's Law and the curvature of the top surface at each such position, the refraction angle θ_i was calculated for each i th ray. Since the travel time in the bubble as assumed by the OCT device was correct, as the medium was air, the corrected bottom surface of the bubble was found by traveling the original length of each projected ray but at the correct angle for that ray. The original length of each projected ray is referred to as r . Thus in effect each location on the measured bottom surface was rotated by pivoting on its corresponding parallel ray around the entry point of that ray into the bubble at corrected top surface, and the predicted angle for that ray. The corresponding coordinates of the corrected top surface, were thus transformed to find the coordinates of the corrected bottom surface, referred to as (X_2, Z_2) .

$$\begin{aligned} X_2 &= r \sin(\theta) + X_1 \\ Z_2 &= r \cos(\theta) + Z_1 \end{aligned}$$

After the correct location of both top and bottom surfaces were calculated, an ellipse was fitted to these locations to predict the entire bubble surface, then that shape was compared to the corresponding CCD images.

3. Results and discussion

The CCD image in Fig. 4a shows the true shape of the bubbles within the raft, with each bubble being nominally a sphere. However, in the OCT image in Fig. 4b, the lower surfaces of the spheres have a smaller radius of curvature than the top surfaces, resulting in a discontinuity in the apparent bubble surface, leading to a shape that can be described as a shield or double wall. This is evident in Fig. 4c where the OCT image (red plane) is registered to the corresponding CCD image (green plane).

Figure 6 (a-d) shows the results of the ray tracing methods; Figs. 6a and c predict the errors arising from refractive effects in OCT (forward ray tracing) and Figs. 6b and d display corrections (inverse ray tracing). The yellow dashed line shows the edge at which rays enter the top surface of the milk solution-mixture. The uncorrected top bubble surface in OCT was found to fit an ellipse, which also describes the distance from the yellow line and is shown in green. The uncorrected top bubble surface is superimposed on the CCD image in Fig. 6c, where it has a tighter curvature than the actual bubble surface. By dividing the z -coordinate by 1.33, this elliptical surface is translated toward the edge, and a corrected thickness and bubble top surface is obtained. This can be compared to the original OCT image (Figs. 6a, b) and the CCD image in Fig. 6d, although the milk solution-mixture edge is rather diffuse under CCD. However, note that the top bubble surface shape is nearly identical to that obtained under CCD, after correction via inverse ray tracing. Using the CCD image (Fig. 6c) and a liquid refractive index of 1.33 as input, forward ray tracing predicts a distorted bottom surface, denoted by the red line in Figs. 6a and c.

Note that the predicted bottom surface artifact falls on the experimentally-observed OCT results (Fig 6a) closely. This prediction also agrees, qualitatively, with previous observations in the literature [18]. In addition, the artifacts agree with a fully computational model of OCT on a hexagonal porous material, using a finite difference time domain (FDTD) that approximates Maxwells equations [23, 24]. Using the correct shape of the top surface and the OCT-observed shape of the bottom surface as input, and applying the algorithm described in the methods section, a corrected bottom surface is obtained, and shown in Figs. 6b, d. Note the significant difference between the corrected model line and the OCT artifact (Fig. 6b) and also the strong similarity between the corrected bottom surface and the actual CCD image (Fig. 6d.)

As shown in previous studies [18], the artifacts from OCT can lead to under-estimation in alveolar volume. We observe a similar phenomenon, and by image analysis the error is approximately 20 %. Previous studies reported errors of 26 % but the difference between methods could be attributed to methods of image analysis. There are slight mismatches between the corrected OCT surfaces when overlaid on the CCD, but we can attribute this to errors in registration of the original images. In addition, the current exercise utilizes soap bubbles that are approximately 250 μm in diameter, which is larger than typical alveolar size. However, prediction of artifacts, and their correction using ray tracing should continue to be applicable at smaller sizes. Finally, as this has been experimentally verified, it would be a reasonable exercise to approximate errors that could be obtained on alveoli of 100 μm or smaller diameter. In addition, this method would be applicable to other highly porous heterogeneous materials, including aerogels, or synthetic liquid foams.

4. Conclusion

Errors that arise from imaging heterogeneous, high porosity materials using OCT have been observed, predicted and corrected in this paper by recourse to a ray tracing approach. The Bragg Nye bubble raft was shown to be a plausible phantom for alveoli, as the geometry and refractive properties are similar. Single bubbles, or the first layer of bubbles, were addressed in this paper.

However, smaller bubbles or different scattering behavior of the liquid from which the bubbles arise would presumably allow imaging of successive layers, and analysis of artifacts under OCT. In addition, non-spherical 'bubbles' could possibly be produced by constraining the top and bottom of the raft, for future study. Moreover, the analysis presented here, while focusing on lung, could also be used in highly porous gels or foams.

